Check for updates

A curtain purification system based on a rabbit fur-based rotating triboelectric nanogenerator for efficient photocatalytic degradation of volatile organic compounds†

Dehong Yang,‡[a] Zhaoqi Liu,‡[b,c] Peng Yang,[b,c] Ling Huang,[a] Fengjiao Huang,[a] Xinglin Tao,[b,c] Yuxiang Shi,[b,c] Rui Lei,[b] Jiazhen Cao,[d] Hexing Li, [ID] [a,e] Xiangyu Chen [ID] *[b,c] and Zhenfeng Bian [ID] *[a]

Efficient removal of air pollution caused by volatile organic compounds (VOCs) and particulate matter (PM) through distributed energy collected from the environment is an effective strategy to achieve both energy conservation and better air quality. Herein, a curtain purification system based on a rabbit fur-based rotary triboelectric nanogenerator (RR-TENG) and a collaborative photocatalysis technology was designed for indoor air purification. The high electrostatic field from RR-TENG enhances formaldehyde adsorption, while it can also efficiently adsorb $PM_{2.5}$ simultaneously. More interestingly, the ultrahigh electric field provided by RR-TENG promotes the separation of photogenerated electron–hole pairs of the g-C_3N_4/TiO_2 composite photocatalyst, generating more superoxide radicals ($\cdot O_2^-$), hydroxyl radicals ($\cdot OH$), and holes (h^+) and thereby improving the photocatalytic efficiency. In a simulated reaction chamber of 9 L, the formaldehyde removal rate of the system can reach 79.2% within 90 min and RR-TENG rapidly reduces $PM_{2.5}$ from 999 μg m^{-3} to 50 μg m^{-3} within 60 s. This study proposes a curtain purification system integrating the function of energy collection and photocatalytic purification, which can be applied for improving air quality and human health.

1. Introduction

For a long time, the development of urbanization has been inseparable from fossil fuels, which has led to many problems, such as environmental pollution and energy shortage. In the living environment, air pollution caused by volatile organic compounds (VOCs) and particulate matter (PM) affects people's lives and industrial production.[1] Formaldehyde (HCHO), mainly coming from building materials, decoration materials, wooden furniture, and cigarettes,[2] is classified as a type of group 1 carcinogenic VOC that seriously threatens human health.[3] At present, the main methods of indoor formaldehyde treatment include physisorption and photocatalytic oxidation.[4,5] Physisorption has limited absorptivity and produces secondary pollution easily. Alternatively, heterogeneous photocatalysis is a promising technology to remove VOCs and can achieve high efficiency and environmental protection.[6] In this respect, the development of new catalysts with higher photocatalytic performance, nontoxicity, and low cost is crucial for degrading VOCs. Typical photocatalytic semiconductor materials are TiO_2,[7] ZnO,[8] WO_3,[9] CdS,[10] $BiVO_4$,[11] *etc*. The TiO_2 photocatalytic semiconductor material is considered as one of the most promising candidate materials for the degradation of organic pollutants.[12] However, its photogenerated electron–hole pairs are easy to recombine, which leads to its limited photocatalytic activity.

On the other hand, previous studies have found that an external electric field can enhance the separation of photogenerated electron–hole pairs, leading to an improved photocatalytic effect. However, this method often consumes con-

[a]*MOE Key Laboratory of Resource Chemistry and Shanghai Key Laboratory of Rare Earth Functional Materials, Shanghai Normal University, Shanghai 200234, China. E-mail: bianzhenfeng@shnu.edu.cn*

[b]*CAS Center for Excellence in Nanoscience, Beijing Key Laboratory of Micro-nano Energy and Sensor, Beijing Institute of Nanoenergy and Nanosystems, Chinese Academy of Sciences, Beijing 100083, China. E-mail: chenxiangyu@binn.cas.cn*

[c]*College of Nanoscience and Technology, University of Chinese Academy of Sciences, Beijing 100049, China*

[d]*Key Laboratory for Advanced Materials and Joint International Research Laboratory of Precision Chemistry and Molecular Engineering, School of Chemistry and Molecular Engineering, East China University of Science and Technology, Shanghai 200237, China*

[e]*Shanghai University of Electric Power, Shanghai 200090, China*

†Electronic supplementary information (ESI) available. See DOI: https://doi.org/10.1039/d3nr00507k

‡These authors contributed equally to this work.

siderable electric energy.[13] In this case, by combining a triboelectric nanogenerator (TENG)[14–17] with the photocatalysis technique, the concept of a self-powered filtering method for removing pollutants can be a promising approach.[18] In order to enhance gaseous acetaldehyde absorption and degradation in photocatalyst systems, researchers used a simple and practical piston-based triboelectric nanogenerator (P-TENG) as the external electric field.[19] The electrostatic field generated by TENGs can also be used for dust removal to reduce PM in air. A self-powered high-voltage charging system based on a biomimetic hairy-contact triboelectric nanogenerator (BHC-TENG) also has the ability to adsorb PM persistently.[20] Moreover, a radial piston TENG-reinforced fiber air filter has been developed for the self-powered removal of particles.[21] Thus, improving the photocatalytic efficiency using TENGs is an effective strategy.

In this paper, a curtain purification system integrating energy collection and photocatalysis is proposed, which achieves the dual effects of formaldehyde degradation and $PM_{2.5}$ removal. The curtain purification system was designed based on a rabbit fur-based rotary triboelectric nanogenerator (RR-TENG) and a composite Z-type photocatalyst (g-C_3N_4/TiO_2). The formaldehyde removal rate of the system can reach 79.2% within 90 min, which is 13% higher than that of the uncharged system. The electron spin resonance (ESR) technique demonstrates that the external electric field from RR-TENG can promote the separation of electron–hole pairs in the g-C_3N_4/TiO_2 composite photocatalyst, realizing a higher removal efficiency. Meanwhile, RR-TENG can rapidly reduce $PM_{2.5}$ from 999 μg m^{-3} to 50 μg m^{-3} in a simulated reaction chamber of 9 L in 60 s, which is only 1/21 of the natural precipitation time. Besides that, when RR-TENG has run for 3 min, the definition of the reaction chamber changes from turbid to clear. Therefore, a curtain purification system based on the integrated technology of RR-TENG and photocatalysis was designed, which can not only fully utilize mechanical energy and solar energy, but also achieve efficient removal of both formaldehyde and $PM_{2.5}$, indicating an effective way to control indoor air conditions.

2. Experimental sections

2.1 Synthesis of the photocatalyst

g-C_3N_4/TiO_2 was prepared by a simple mixed calcination method, which was based on previously reported articles.[22] Urea (1 g) was dissolved in ultrapure water (DI, 10 mL), stirred and dissolved completely. According to the weight percentage (wt%) of 1 : 1, commercial TiO_2 nanoparticles (1 g) were mixed in it, stirred for 10 min, and then ultrasonically dispersed for 30 min. The mixture was placed into a thermostat water bath at 60 °C and stirred until dry. The obtained sample was loaded into a crucible, sealed, and calcined at 550 °C in a muffle furnace (heating rate of 10 °C·min^{-1}) for 60 min. The sample was removed for grinding when its temperature dropped to the environment, and a yellowish g-C_3N_4/TiO_2 was obtained.

2.2 Treatment of fabric

First, the fabric (polyester cloth) purchased from the market was pretreated. The main steps of pretreatment include degreasing, roughening and cleaning. Degreasing and roughening: the fabric was dipped in NaOH (AR, 200 g L^{-1}) solution at a constant temperature (70 °C) for 30 min. Cleaning: ultrasonic cleaning with acetone, alcohol, and ultrapure water in turn. Second, the fabric was made into specific curtains, and the main steps were preparation and spraying. Preparation: the g-C_3N_4/TiO_2 composite photocatalyst (0.1 g) was dissolved in a mixed solution of absolute ethanol (1 mL) and conductive liquid (PEDOT/PSS OE-001, 3 mL) and dispersed sonically for 30 min. Spraying: the dispersed mixture was packed in a highly atomized spray gun (HD-130, 0.3 mm) and sprayed 10 cm above the treated fabric. In particular, the fabric was sprayed for 10 s and then dried in an oven at 60 °C repeatedly. The curtain (100 × 100 mm) with purification function and high conductivity can be obtained. The transparent curtain cloth on the other side was a gauze curtain with a silver thread (bought from the market).

2.3 Fabrication of the RR-TENG

The RR-TENG was composed of two parts: a rotor and a stator. Rotor part (fur disk): first, a number of whole rabbit furs were obtained from the market (Hebei Houqiang Home Textiles Co., LTD), and rabbit furs with a uniform density (back part) were screened out and cut into the corresponding fan shapes (according to the spacing). The rabbit fur with a length of 6 mm was treated with a shaver (including a 6 mm positioning comb) and then blown by an air compressor (TW5501S). The acrylic (3 mm) was cut into the desired shape using a laser cutting machine, and then the rabbit fur was glued to the cut acrylic with double-sided tape (3 M LSE). Stator part (electrode disk): the electrode was fabricated using the PCB technique, and the designed disk was composed of an FR-4 substrate (r = 138 mm) and copper layers (35 μm). The patterned Cu sectors were divided into two groups, which were electrically connected. The spacings between adjacent electrodes were designed to 3, 6 and 9 mm. Then, polytetrafluoroethylene (PTFE, 80 μm) films adhered on the copper layers as a triboelectric layer. The high-voltage rectifier consisted of four high-voltage diodes, and the withstand voltage value of each diode was 20 kV.

2.4 Fabrication of the reaction chamber

Two simulated reaction chambers (300 × 200 × 150 mm, V = 9000 cm^3 = 9 L) were assembled with acrylic. One was a reaction chamber containing quartz slices (220 × 170 mm) for formaldehyde degradation, and the other was a reaction chamber for dust removal. A tiny fan was built inside to recycle gas, and screws were used to seal the reaction chamber.

2.5 Degradation of formaldehyde gas

Before the reaction chamber was sealed, 36% diluted formaldehyde solution (HCHO, 5 μL) was injected into the box, and a tiny fan was used to recycle the sealed air (0.6 m s^{-1}, VC816B).

After a solvent evaporation time of 3.5 h, the formaldehyde concentration was stable at 1.5 ± 0.05 ppm (1 ppm = 1 mg m^{-3}). The fabric reached an adsorption–desorption equilibrium. A 365 nm LED was irradiated vertically upon the fabric at a distance of 10 cm (9.25 mW cm^{-2}, CEL-NP2000), and the RR-TENG cooperated with the photocatalytic degradation of formaldehyde. The gas formaldehyde concentration was detected using a British formaldehyde detector (PPM Tech. Ltd, HTV-m) in the reaction chamber.

2.6 Electrical measurement and characterization

The open-circuit voltage was measured using a high-speed electrostatic voltmeter (Trek Model 341B). A programmable electrometer (Keithley 6514) was used to test the transferred charge and the short-circuit current. A field emission scanning electron microscope (FESEM, HITACHI/SU8020) was used for morphology characterization. A field emission transmission electron microscope (FETEM, FEI/Tecnai G20 F20 S-TWIN TMP) and energy dispersive spectroscopy (EDS) were used for elemental analysis. An X-ray diffractometer (XRD, Panalytical Xpert3 Powder, Cu Kα radiation) was used to characterize the crystal structures of the photocatalysts. An X-ray photoelectron spectrometer (XPS, ESCALAB 250Xi) was used with a monochromatic Al Kα excitation source (1486.6 eV). UV-vis diffuse reflectance spectra (DRS) were obtained using a spectrophotometer (Shimadzu UV 3600) with an integrating sphere attachment and with BaSO$_4$ as the reflectance standard. The specific surface area and pore size distribution of the photocatalyst were analyzed using a research-type automatic gas adsorption instrument (BET, Kingep/V-Sorb 2800TP). Electron paramagnetic resonance spectroscopy (ESR/EPR, Bruker A300, Germany) was used to detect the role of free radicals and holes in the self-powered photocatalytic process by analyzing the sample under dark, light, light and electric field conditions for 5 min.

3. Results and discussion

3.1 Application scenario of the curtain purification system

Decoration materials, wooden furniture, kitchen fumes, and cigarette smoke are the major sources[23] of indoor formaldehyde and PM$_{2.5}$, which may cause irreversible damage to people.[24] Herein, we demonstrate that the RR-TENG for distributed energy collection synergizing photocatalytic technology effectively degrades formaldehyde and removes particulate matter. Fig. 1a shows an application scenario for the indoor curtain purification system integrating with the function of energy collection and photocatalytic purification (inset: schematic diagram of formaldehyde degradation). The distribution of flake g-C$_3$N$_4$ and the nanoparticle TiO$_2$ composite photocatalyst can be observed. As marked in Fig. 1b, the composite photocatalyst is mixed with the conductive liquid and sprayed on the fabric. A SEM image of the g-C$_3$N$_4$/TiO$_2$ composite photocatalyst in the curtain is shown in Fig. 1c. Fig. 1d shows the micromorphology of the PTFE film, which is used as a

dielectric material to generate electric energy by friction with the rabbit hair. In general, the time and proportion of curtains exposed to sunlight are very long, so curtains with a large contact area are a good choice as the carrier of photocatalysts. The inspiration for using the treated fabric as a curtain comes from real life. Here, the curtain purification system is mainly composed of a RR-TENG, two curtains (100 × 100 mm) and a simulated reaction chamber (9 L). The size of the curtain and the simulation reaction room was designed according to the proportion of the size of the room and the curtain in real life. The two output ends of the distributed RR-TENG, which collects mechanical energy in the forms of wind, water flow and human motion,[25–28] are rectified by high-voltage diodes and connected to two curtains on the opposite side by wires (Fig. S1†). Thus, a strong electrostatic field is generated between a conductive curtain loaded with g-C$_3$N$_4$/TiO$_2$ and a gauze curtain containing a silver wire (commercial curtain). However, formaldehyde molecules and PM$_{2.5}$ are constantly adsorbed on two curtains in the indoor air. Through sunlight irradiation, the conductive curtain loaded with g-C$_3$N$_4$/TiO$_2$ continuously purifies formaldehyde. However, a small number of PM$_{2.5}$ and formaldehyde adsorbed the gauze curtain can be removed by water washing. It can also be slowly released and repeatedly absorbed by the conductive curtain under the continuous action of the RR-TENG. On the one hand, the electrostatic field further enhances the adsorption of formaldehyde and the efficiency of the photocatalytic degradation of formaldehyde under light conditions; meanwhile, it can also quickly remove PM$_{2.5}$ from indoor air. According to the schematic diagram of formaldehyde degradation, the curtain purification system can be extended to the degradation of other VOCs (Fig. 1e). More free radicals and holes are generated through the RR-TENG, which undergo redox reactions with volatile organic compounds and generate CO$_2$ and H$_2$O inside. This system realizes purification from polluted air to clean air and achieves the purpose of clean energy and the environment.

3.2 Materials characterization

TiO$_2$ is widely used because of its high photocatalytic activity, nontoxicity, low cost and stable chemical properties, but there are also two major defects.[29–31] The first point is the high recombination rate of photogenerated electron–hole pairs. This reduces its photocatalytic performance. The second point is that its bandgap is 3.2 eV, which requires more external energy for electrons in the valence band to transition to the conduction band. Due to its low band gap (2.70 eV), low cost, good physicochemical stability, and abundance, g-C$_3$N$_4$ is considered a promising metal-free photocatalyst.[32] Therefore, the method of semiconductor recombination is used to improve photocatalytic performance in this paper.[33]

Using urea and commercial TiO$_2$ as raw materials, a Z-type g-C$_3$N$_4$/TiO$_2$ composite photocatalyst is successfully prepared by a simple hybrid calcination method (Fig. S2†). To determine the phase structure and composition of each sample, X-ray diffraction (XRD) was performed on g-C$_3$N$_4$/TiO$_2$, TiO$_2$, and g-C$_3$N$_4$. Fig. 2a shows that pure g-C$_3$N$_4$ has only two character-
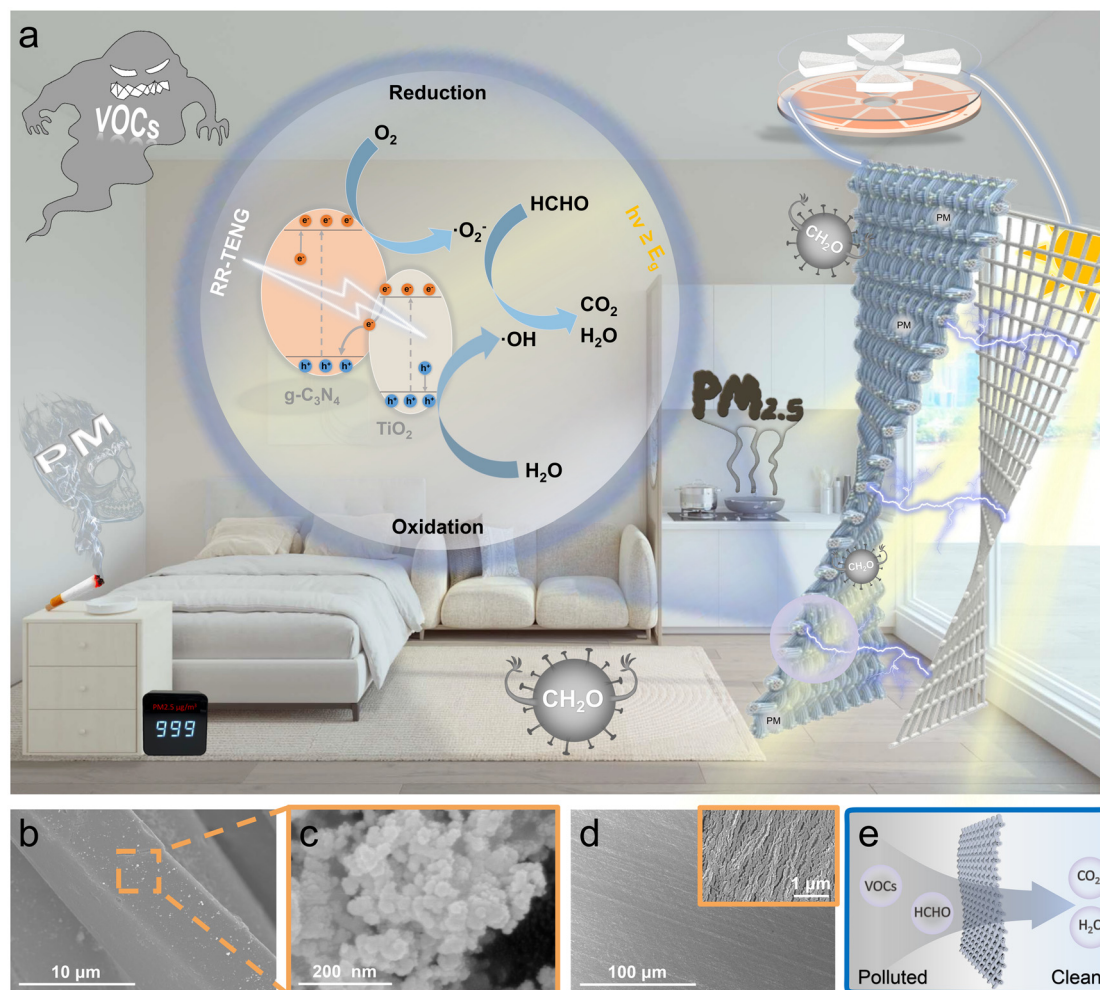
Fig. 1 Demonstration of a curtain purification system integrated with the functions of energy collection and photocatalytic purification. (a) Schematic illustration of the application scenario of the curtain purification system for dedusting and formaldehyde degradation. SEM images of (b) a conductive curtain containing photocatalyst, scale bar: 10 μm, (c) a g-C_3N_4/TiO_2 composite photocatalyst, scale bar: 200 nm and (d) a PTFE film, scale bar: 100 μm (inset, scale bar: 1 μm). (e) Application expansion illustration (conversion of VOCs to CO_2 and H_2O).

istic peaks (2 θ = 12.8°, 27.4°), which are consistent with those reported in the literature.[34] Compared with TiO_2, the g-C_3N_4 component enhances the characteristic peaks of g-C_3N_4/TiO_2 but does not affect the position of the characteristic peaks. This shows that the presence of g-C_3N_4 has little effect on the crystal structure of TiO_2. g-C_3N_4/TiO_2 has no other impurities and has high crystallinity. The g-C_3N_4/TiO_2 and TiO_2 samples show very similar absorption characteristics, indicating that C or N is not incorporated into the crystals of TiO_2 in Fig. 2b, which indicates that the composite material is prepared successfully.[35] Fig. 2c and d show the HRTEM images of g-C_3N_4/ TiO_2, and the scale bar are 20 nm and 5 nm, respectively. The nanoparticle TiO_2 is uniformly wrapped with g-C_3N_4, and the interface is very obvious, which further proves the formation of its heterojunction. The lattice fringes of d = 0.352 nm and d = 0.235 nm are match with the (101) and (001) crystal planes of anatase TiO_2, respectively. Due to the semi-crystalline pro-

perties of g-C_3N_4, it is difficult to observe the lattice fringes. As marked in Fig. 2e, O, Ti, N and C elements are uniformly distributed in g-C_3N_4/TiO_2, thus the result further demonstrates the preparation of the composite photocatalyst successfully. All XPS data are scaled to the band energies of C 1 s. The XPS high-resolution spectrum shows the presence of O, Ti, N and C elements (Fig. 2f), indicating that g-C_3N_4/TiO_2 is mainly composed of O, Ti, N and C elements. The peaks of N, Ti, O, and C of g-C_3N_4/TiO_2 are slightly shifted in Fig. 2g–j. Note that no obvious Ti–C and Ti–N incorporations were found in g-C_3N_4/ TiO_2.[34] This indicates that g-C_3N_4 is only deposited on the surface of TiO_2 in a heterojunction structure, which corresponds to the results of TEM. In the grid, it further shows that g-C_3N_4 is only deposited on the surface of TiO_2 in the composite photocatalyst, and the particles are not incorporated into the lattice of TiO_2. Based on the above description, the results of XRD, UV-vis, HRTEM, EDS and XPS are consistent.
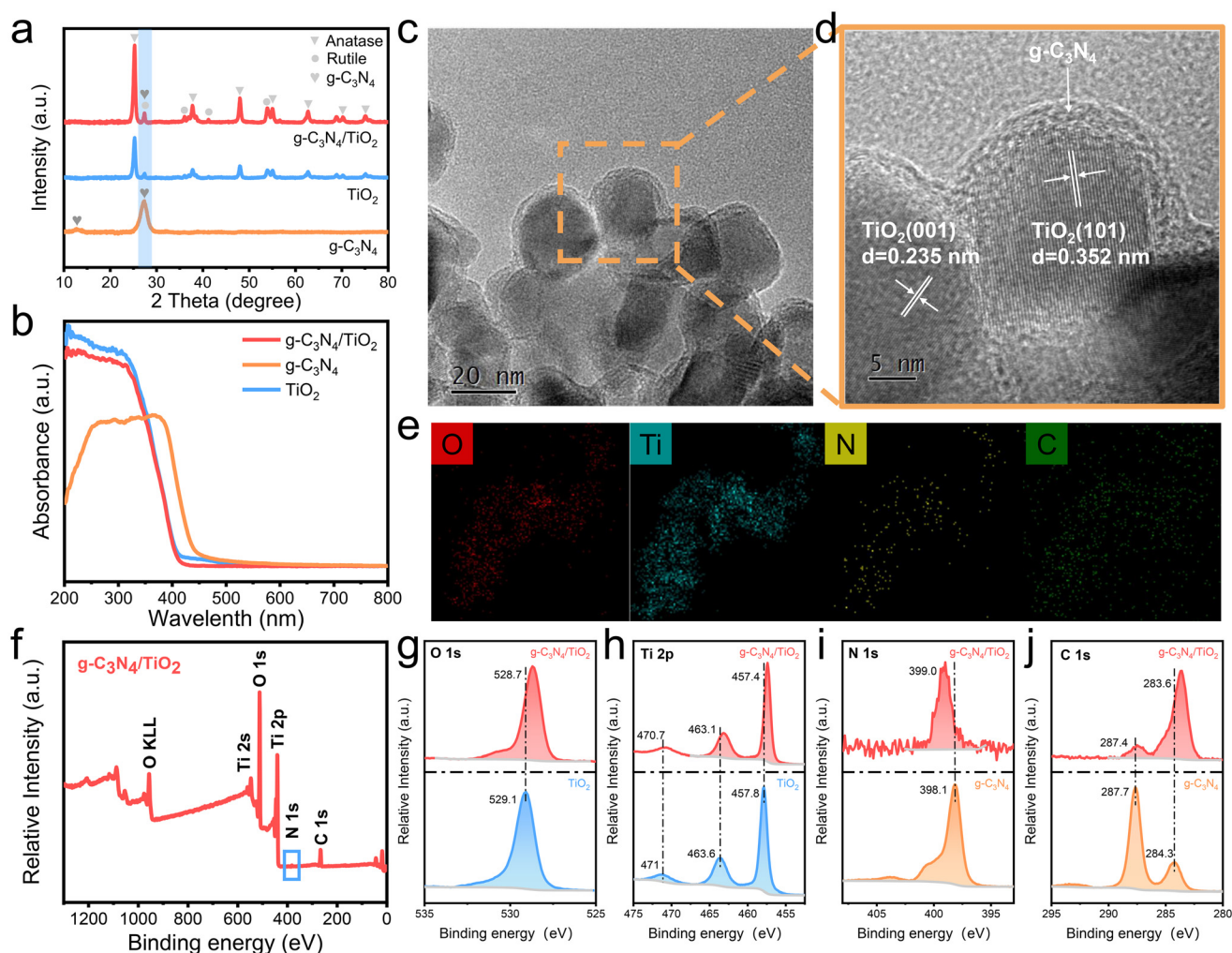
Fig. 2 Characterization tests of photocatalysts. XRD patterns (a) and UV-vis absorption spectra (b) of photocatalysts. (c) TEM image of g-C$_3$N$_4$/TiO$_2$, scale bar: 20 nm. (d) Crystalline lattices of g-C$_3$N$_4$/TiO$_2$, scale bar: 5 nm. EDS elemental mapping (e) and the XPS main spectrum (f) of g-C$_3$N$_4$/TiO$_2$. XPS spectra of O$_{1s}$ (g), Ti$_{2p}$ (h), N$_{1s}$ (i) and C$_{1s}$ (j) in g-C$_3$N$_4$/TiO$_2$.

3.3 Process of curtain preparation

The curtain with purification function and high conductivity is the key element for this system, in order to realize the self-powered function of the RR-TENG. Thus, we used the spraying method to obtain the fabric as curtains that can link the electricity and photocatalysis. The commercial fabric was pretreated to enhance the hydrophilicity of the fabric (Fig. S3†). Fig. 3a shows the production process and the partial enlargement of the curtain. A mixture of g-C$_3$N$_4$/TiO$_2$, conductive solution and anhydrous alcohol was loaded into the spray gun and then sprayed 10 cm above the fabric (Fig. S4a†). The finished curtain can be obtained after drying (Fig. S4b†). To observe the g-C$_3$N$_4$/TiO$_2$ loading more intuitively, the surface morphology of the fabric was characterized. SEM images of curtains with different treatments are shown in Fig. 3b–d, and the scale bar is 100 μm, where the inset shows the SEM image of a single fiber with a scale bar of 5 μm. The pretreated fabric has multiple fibers and no impurities on the surface (Fig. 3b). Its mor-

phology is similar to that of the fabric containing only conductive liquid (Fig. 3c). Tested using a multimeter, the fabric containing only conductive liquid has excellent electrical conductivity. As can be seen in Fig. 3d, g-C$_3$N$_4$/TiO$_2$ is dispersed on the fibers of the finished curtain containing photocatalysts and conductive solution. This method increases the specific surface area of the photocatalyst and accelerates the reaction. This further indicates that the g-C$_3$N$_4$/TiO$_2$ composite photocatalyst is successfully loaded on the curtain.

3.4 Design and output performance of the RR-TENG

As a promising energy harvesting technology, TENGs can convert mechanical energy into electricity.[36,37] Meanwhile, the ultrahigh electrostatic generated from TENGs can promote a series of catalytic reactions without consuming other energy sources. As shown in Fig. 4a, the operation principle of the RR-TENG is based on the coupling effect between triboelectrification and electrostatic induction between two different
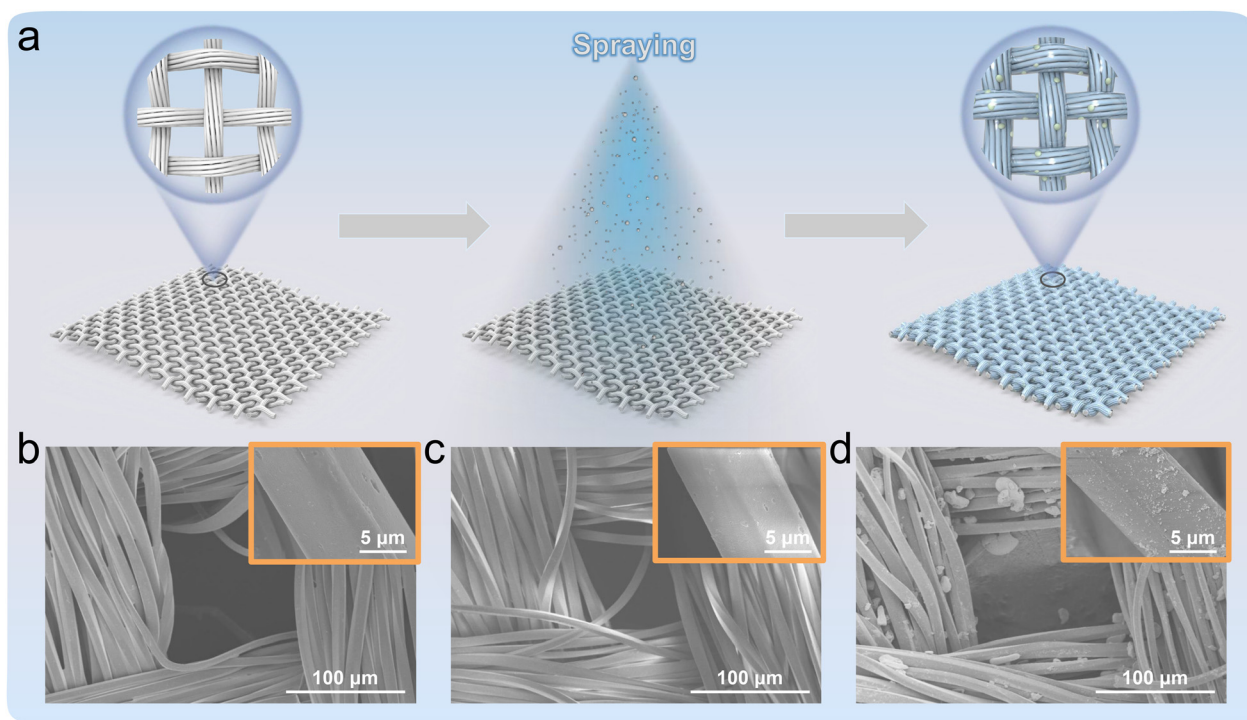
Fig. 3 Preparation illustration of a conductive curtain containing photocatalyst. (a) Preparation illustration of a conductive curtain containing g-C_3N_4/TiO_2. SEM images of (b) the curtain after pretreatment, (c) conductive curtain, and (d) conductive curtain containing g-C_3N_4/TiO_2, scale bar: 100 μm (inset, scale bar: 5 μm).

materials.[38] To illustrate its working principle in detail, six different states of the RR-TENG are listed (Fig. 4a(i–vi)). State (i) shows the initial state, in which the rabbit fur layer is just placed on the left electrode. When the rabbit fur layer is in contact with the PTFE film, the electron transfer process leads to the generation of positive charges on the rabbit hair and negative charges on the surface of the PTFE film. Due to charge conservation, the total triboelectric charges of the rabbit fur layer and PTFE film are equal.[39] As shown in states (ii) and (iii), when the rabbit fur layer rotor slides counterclockwise and rotates relative to the stator, the positive and negative charges generated by contact electrification are separated, which causes a potential difference between two triboelectric layers and generate a strong output voltage to the external circuit. When the rabbit fur layer is rotated to the right electrode (state (iv)), triboelectric positive and negative charges are generated again. After the rabbit hair layer passes through the entire electrode, the driven electrons flow from the right electrode to the left electrode. A reverse pulse current is generated through an external resistor, and then flows from the left electrode to the right electrode (states (v) and (vi)). When a load is connected between two output electrodes, the induced potential difference drives electrons to flow through the external circuit to balance the electrostatic field generated by the TENG. Due to the periodic structure, the continuous rotation and separation of the rabbit hair layer and the PTFE film produces an AC output.[40]

Soft rabbit hair is not only an excellent friction material but also can reduce the surface wear between materials, which

helps to improve the durability of the device.[39] Because commercially purchased rabbit hair (Fig. S5a†) is too long to frictional movement,[41] it is cut into a depth of 6 mm rabbit fur (Fig. S5b†) and compared its effects in Fig. S5c.† The effect of different spacings of complementary electrodes on the electrical output performance was investigated. The open-circuit voltage (V_{OC}), short-circuit current (I_{SC}), and transferred charge (Q_{SC}) of the RR-TENG with different electrode pitches (L_e) were compared (r = 300 rpm min^{-1}). As shown in Fig. 4b, as the distance increases, V_{OC} also increases, and the V_{OC} value of the RR-TENG (L_e = 9 mm) can reach 20 kV. However, it is shown in Fig. 4c and d that the I_{SC} and Q_{SC} value of the RR-TENG decrease with increasing spacing.[40] A RR-TENG with the same grid number and different spacings (L_e = 3, 6 and 9 mm) is shown in Fig. 4e. Taking the RR-TENG (L_e = 9 mm) as the target TENG in this work, the TENG can provide a stronger high electrostatic field to achieve a stronger air governance effect.

As can be seen in Fig. 5a–c, the output performances at different rotational speeds (r = 50, 100, 150, 200, 250 and 300 rpm min^{-1}) were tested. Based on the theoretical analysis, as long as the device structure and initial surface charge density remain unchanged, V_{OC} is not affected by speed.[42] As indicated in Fig. 5a, V_{OC} may increase with increasing rotational speed. This is because in the actual test process, the increase of the rotational speed may suppress the charge leakage phenomenon, and the rotational speed has a certain influence on the voltage. Fig. 5b and c show that I_{SC} and Q_{SC}, and I_{SC} increase
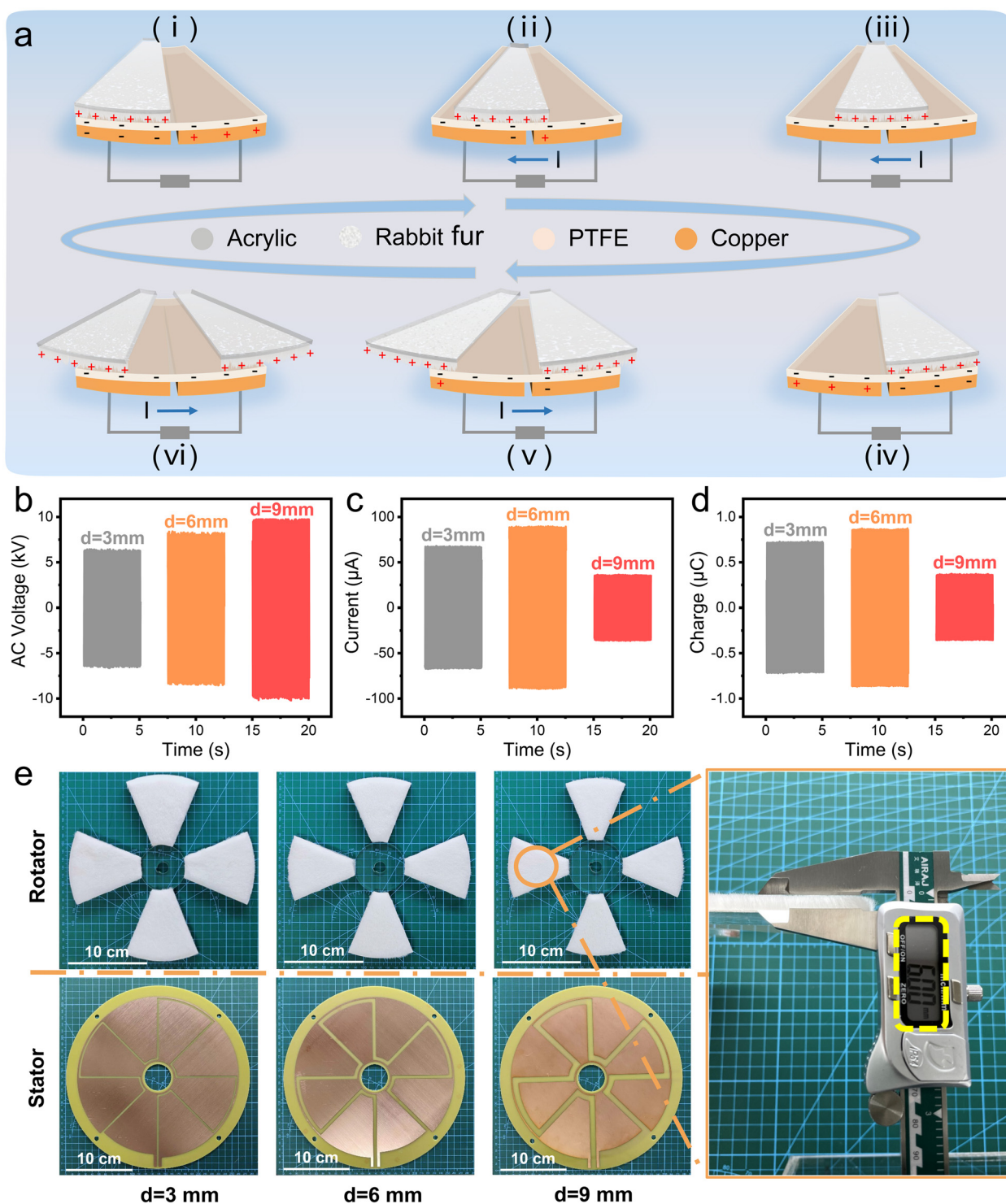
Fig. 4 Comparison of the electric output performance of a RR-TENG with different spacings. (a) Schematic illustration of the working principle of the RR-TENG. The open-circuit voltage (b), the short-circuit current (c) and the transferred charges (d) of the RR-TENG with spacings of 3, 6, and 9 mm. (e) Photographs of the RR-TENG structure with spacings of 3, 6 and 9 mm (scale bar: 10 cm).

as the speed increases. The Q_{SC} numerical balance reaches the saturation state of the PTFE film.[43] The structure of the RR-TENG for the degradation test is shown in Fig. 5d. The device is mainly composed of three parts: an electrode plate, a PTFE film, and a rabbit hair layer, as we explained in the previous part. The PTFE film is pasted on the electrode plate as a stator, and the rabbit fur is pasted on the acrylic plate as a rotor. To investigate the stability of the TENG, the voltage output of the RR-TENG was tested after 2000 times operation. As shown in Fig. S6,† the output voltage can maintain 90.9%
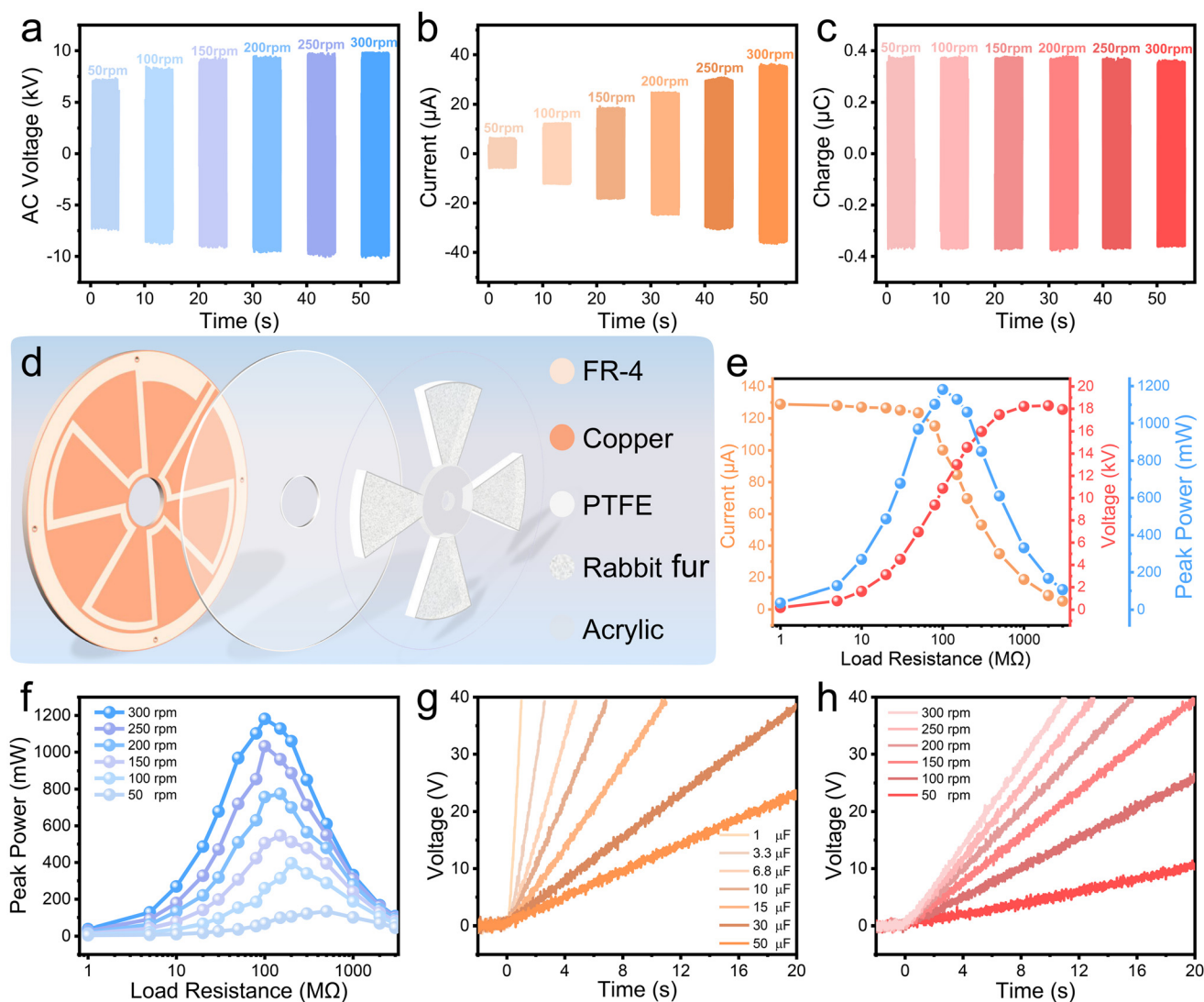
Fig. 5 Basic output performance of a RR-TENG with a spacing of 9 mm. The open-circuit voltage (a), the short-circuit current (b) and the transferred charges (c) of the RR-TENG with a spacing of 9 mm at different rotation speeds (r = 50, 100, 150, 200, 250 and 300 rpm min^{-1}). (d) Structural design drawing of the RR-TENG. (e) The peak power curve of the RR-TENG (r = 300 rpm min^{-1}). (f) Peak power curves of the RR-TENG with a spacing of 9 mm at different rotation speeds (r = 50, 100, 150, 200, 250 and 300 rpm min^{-1}). (g) Capacitors charging curves by the RR-TENG (r = 300 rpm min^{-1}). (h) Charging speed of the RR-TENG at different rotation speeds (U = 30 μF).

of the output performance. Here, the microscopic morphology images of PTFE before (Fig. S7a†) and after (Fig. S7b†) friction were compared and analyzed, and the results illustrate that the surface topography of PTFE does not change. The dependences of V_{OC}, I_{SC} and peak power on the external resistance are shown in Fig. 5e. Obviously, the maximum instantaneous peak power can reach 1200 mW under an external matching resistance of 110 MΩ (r = 300 rpm min^{-1}). The calculation of the instantaneous output power (P) is shown as eqn (1):

$$P = \frac{U_t^{\,2}}{R} \tag{1}$$

where U_t is the open circuit voltage of the RR-TENG and R is the resistance of the external circuit. In addition, the influence

of different rotation speeds on the peak power was also investigated. As the rotation speed increases in Fig. 5f, the maximum instantaneous peak power of the RR-TENG also increases, which is also related to the suppression of charge leakage. Using the circuit diagram shown in Fig. S8,† different charging profiles of the RR-TENG were tested and are presented in Fig. 5g and a 30 μF capacitor can charge to 40 V in 20 s (r = 300 rpm min^{-1}). Under a capacitor of 30 μF, the charging efficiency can be further improved by increasing the rotation speed (Fig. 5h).

3.5 Performance analysis of formaldehyde degradation

To simulate the indoor environment, a 9 L reaction chamber with one side of quartz glass was made by using an acrylic plate (Fig. S9†). After the volatilization of liquid formaldehyde,

gaseous formaldehyde is used as a simulated indoor volatile organic compound to evaluate the ability of system to degrade formaldehyde. To improve the efficiency of the photocatalyst, a composite Z-type photocatalyst (g-C_3N_4/TiO_2) was developed in this study. As shown in Fig. 6a, the photocatalytic activity of g-C_3N_4/TiO_2 is higher than that of TiO_2 alone during the whole reaction process. As the effective modification of TiO_2, adding g-C_3N_4 can promote the separation of photogenerated electron–hole pairs, which makes g-C_3N_4/TiO_2 exhibit a higher photocurrent response than single TiO_2 (Fig. S10†).[44] A certain amount of formaldehyde solution was added into the reaction chamber, and the solution was volatilized for 180 min to reach the equilibrium of adsorption–desorption. The adsorption amount changes were tested for the natural sedimentation (without curtains), conductive curtain and conductive curtain

loaded with g-C_3N_4/TiO_2 in Fig. 6b. The curtain has a certain adsorption effect on formaldehyde. It is obvious that the formaldehyde concentration of the photocatalyst-loaded conductive curtain is much lower than that of the conductive curtain, which is due to the adsorption of g-C_3N_4/TiO_2. Compared with TiO_2, the BET surface area of g-C_3N_4/TiO_2 increases, and the adsorption capacity of g-C_3N_4/TiO_2 is further enhanced (Fig. S11†). In Fig. 6c, g-C_3N_4/TiO_2 shows a relatively small loss of photocatalytic activity after three consecutive uses, and the formaldehyde removal rate is still as high as 70% when the third cycle is performed.

As shown in Fig. 6d, the ability to degrade formaldehyde was evaluated by C/C_0 and the concentration of formaldehyde decreased over time. More importantly, the degradation effect of adding the RR-TENG is better than that without the
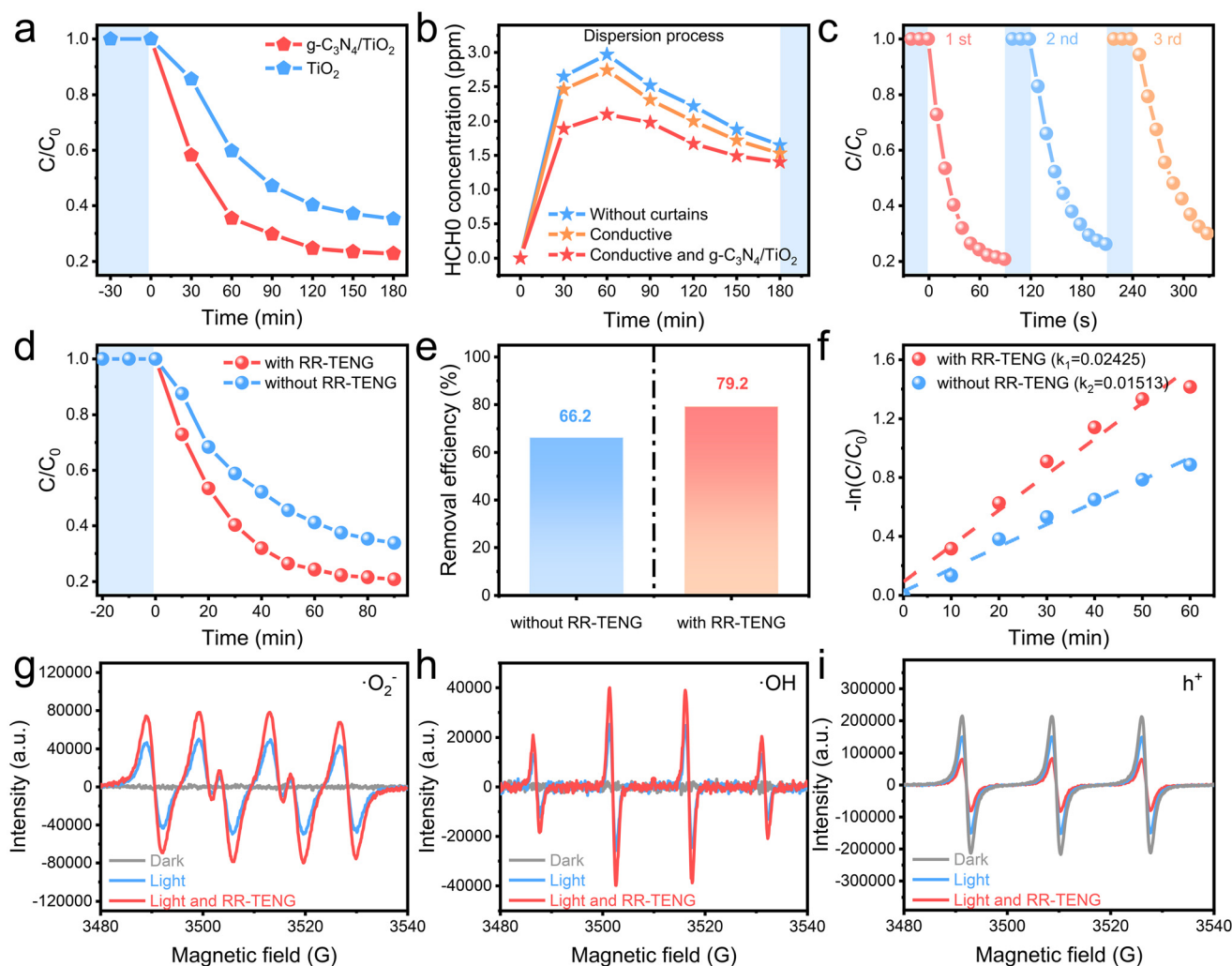

Fig. 6 Process of formaldehyde purification by RR-TENG synergistic photocatalysis. (a) Comparison of the formaldehyde degradation effect between a g-C_3N_4/TiO_2 composite photocatalyst and a TiO_2 photocatalyst. (b) Change of the adsorption capacity of the natural sedimentation (without curtains), conductive curtain and conductive curtain loaded with the g-C_3N_4/TiO_2 composite photocatalyst. (c) Recycling performance of the RR-TENG synergistic photocatalytic degradation of formaldehyde. (d) Comparison of the formaldehyde degradation effect (with and without the RR-TENG). (e) Instantaneous removal rates of gaseous formaldehyde in 90 min (with and without the RR-TENG). (f) Kinetic curve of formaldehyde degradation (with and without the RR-TENG). (g–i) ESR spectra of free radicals and h$^+$ trapped by DMPO ($\cdot O_2^-$ and $\cdot OH$) and TEMPO (h$^+$) under dark, light, and light and RR-TENG conditions for 5 min.

Paper

RR-TENG. Under light irradiation for 90 min, the formaldehyde concentration with the RR-TENG only decreases by 79.2%. However, the formaldehyde concentration without the RR-TENG decreases by 66.2% (Fig. 6e). According to eqn (2), the degradation efficiency (η) of formaldehyde was calculated. The degradation of HCHO in different systems was fitted by a pseudo-first-order kinetic model, which can be expressed as eqn (3). As shown in Fig. 6f, the results show that the reaction rate constant (k_1) of the system with the RR-TENG is larger than that of the system without the RR-TENG (k_2), which

further prove that the RR-TENG plays a positive role in the degradation of formaldehyde. The detailed equation for efficiency evaluation is as follow:

$$\eta\% = (C/C_0) \times 100\% \tag{2}$$

$$\ln(C/C_0) = -kt \tag{3}$$

where C_0 and C are the initial equilibrium concentration of formaldehyde and the actual concentration of dyes at reaction time t, respectively.
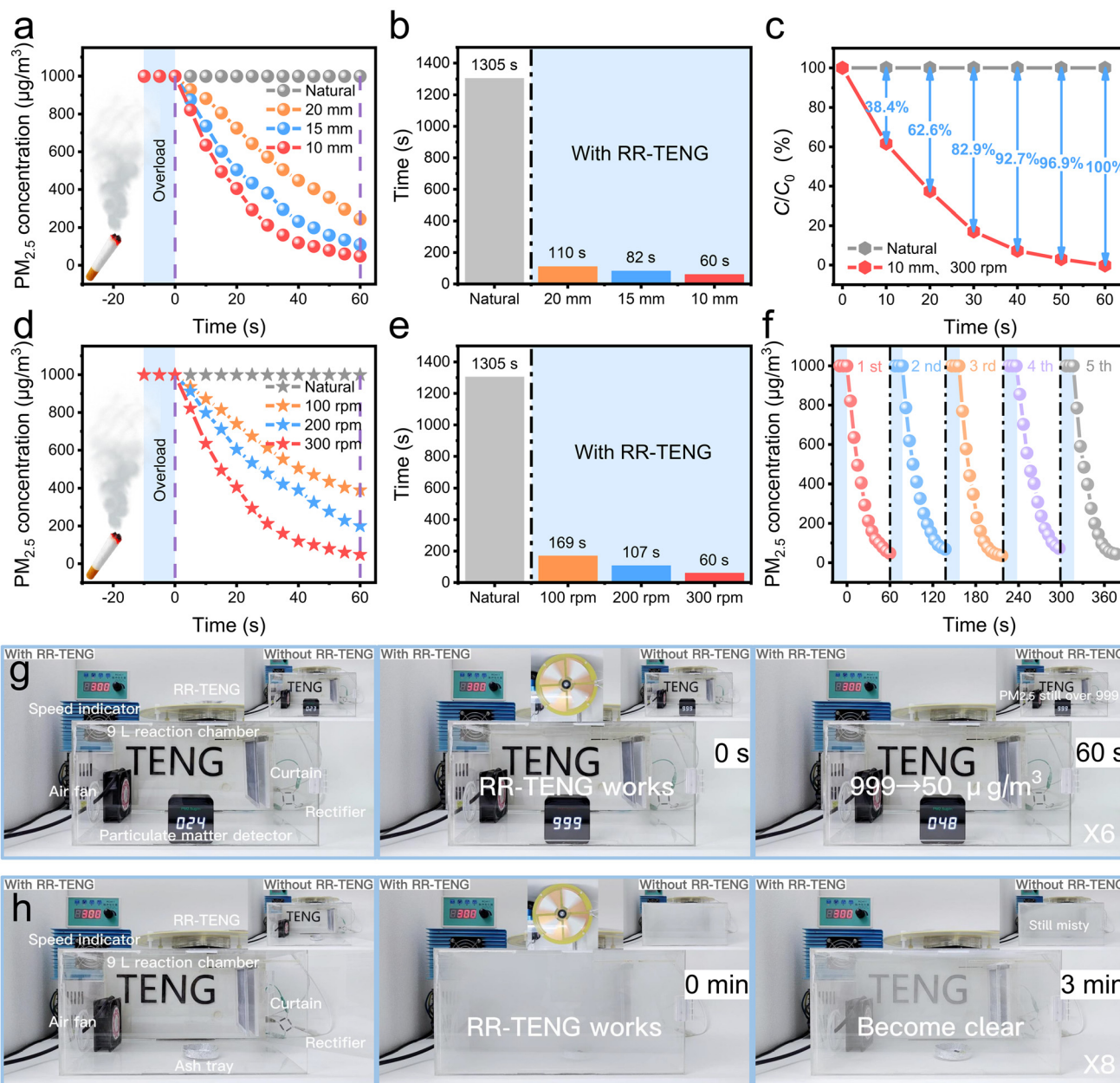

Fig. 7 RR-TENG removal of PM$_{2.5}$ and heavy smog. Removal effect on PM$_{2.5}$ (a) and the comparison of PM$_{2.5}$ removal time (b) with different spacings (r = 300 rpm min^{-1}). (c) PM$_{2.5}$ removal performance (r = 300 rpm min^{-1}, L_c = 10 mm). Removal effect on PM$_{2.5}$ (d) and the comparison of PM$_{2.5}$ removal time (e) at different rotation speeds (L_c = 10 mm). (f) Recycling test of the RR-TRNG for PM$_{2.5}$ removal (r = 300 rpm min^{-1}, L_c = 10 mm). (g) RR-TENG demonstration of PM$_{2.5}$ removal performance. (h) RR-TENG demonstration of heavy smog removal performance.

The radicals and holes generated during the synergistic photocatalytic degradation of formaldehyde by the RR-TENG were explored by electron spin capture (ESR) experiments, and the detailed mechanism was elucidated. Fig. 6g–i show that the active species that play a role in the reaction process are ·OH, ·O_2^- and h$^+$, respectively. Using dimethylpyridine nitrogen oxide (DMPO) and tetramethylpiperidine nitrogen oxide (TEMPO) as free radical scavengers, the ESR signal intensities of ·OH, ·O_2^- and h$^+$ were explored under dark, light, light and RR-TENG conditions. The solution shows no ·OH and ·O_2^- under dark conditions, while ·OH and ·O_2^- can be detected under light conditions for 5 min (Fig. 6g and h). When the light and RR-TENG are applied concurrently, the signals of ·OH and ·O_2^- are stronger than those under light alone, and the intensity order of ·OH, ·O_2^-, and h$^+$ is still light and RR-TENG > light > dark. In addition, Fig. 6i shows a strong signal of the TEMPO collector in the dark. It is observed that the intensity of h$^+$ is weakened when the light and RR-TENG act for 5 min since the holes generate on the composite material neutralized the signal of the TEMPO trapping agent, which weakens the h$^+$ signal.[45] This result indicates that the external electrostatic field provided by the RR-TENG facilitates the separation of electron–hole pairs within the composite[46] and promotes more electrons (e$^-$) and holes (h$^+$) to migrate to the surface of the photocatalyst. The oxidation–reduction reaction with gaseous formaldehyde finally produces nontoxic and harmless CO_2 and H_2O (Fig. S12†). The above results prove that the external electrostatic field provided by the RR-TENG can improve the efficiency of the photocatalytic degradation of formaldehyde.

3.6 Performance analysis of PM$_{2.5}$ removal

In the actual indoor environment, the impact of PM$_{2.5}$ on the human body cannot be underestimated. The electrostatic dust removal technology based on a TENG has the characteristics of high efficiency, low wind resistance, and extremely low ozone generation. In this work, a RR-TENG was designed to clean fine PM in the indoor air. Taking cigarette smoke as the source of PM$_{2.5}$, the removal ability of the system to PM$_{2.5}$ was evaluated. PM$_{2.5}$ was added to a 9 L reaction chamber (>>999 μg m^{-3}), and the fan was turned on to circulate air. After 10 min of stabilization, the effect of different curtain spacings (L_c) on the removal of PM$_{2.5}$ was studied as shown in Fig. 7a (r = 300 rpm min^{-1}). Within 60 s, the curtain (L_c = 10 mm) can quickly remove PM$_{2.5}$ from 999 to 50 μg m^{-3}. However, PM$_{2.5}$ has been in an overload state under natural settlement conditions. According to this result, the order of clearance rate is: 10 mm > 15 mm > 20 mm. This is because the smaller the distance the higher of the voltage of the electrostatic field, and the faster the rate of adsorption of PM$_{2.5}$. The dust removal time (from 999 to 50 μg m^{-3}) of curtains with different spacings was calculated (300 rpm min^{-1}). Obviously, 20 mm takes the longest time (110 s), followed by 15 mm (82 s) and 10 mm (60 s) is the fastest (Fig. 7b). Fig. 7c shows the PM$_{2.5}$ removal efficiency at 0, 10, 20, 30, 40, 50, and 60 s. Under the conditions of the same spacing of 10 mm, the influence of different rotation speeds of RR-TENG on the removal of PM$_{2.5}$ was studied (Fig. 7d). The higher the rotation speed the more obvious of the cleaning effect, and the statistics about time are shown in Fig. 7e. The system has been run 5 times and the performance is still good (Fig. 7f). The photographs of dust removal at 0 s and 60 s are shown in Fig. 7g, and the details of dust removal can be found in Video S1.† In order to see the effect of electrostatic field dust removal more intuitively, the process of the RR-TENG to remove dense smoke was recorded in Video S2.† The smoke of a certain mass of the smoke sheet is dispersed evenly for 2 min. At 0 min, both the reaction chamber with the RR-TENG and the reaction chamber without the RR-TENG remain in a turbid state. Here, the amount of PM is larger than the detecting range of the detector. After starting the operation, the clarity of the RR-TENG reaction chamber increases over time. After 3 min of operation, the reaction chamber becomes clearer and the characters of the TENG behind the reaction chamber can be clearly seen in Fig. 7h. Moreover, the smoke in the chamber without the RR-TENG is still very dense, indicating the contribution of the TENG. Fig. S13† shows the SEM images of the curtain before and after repeated dust removal, while PM$_{2.5}$ is firmly adsorbed on the curtain. This result shows that the external high electrostatic field provided by the RR-TENG can also efficiently remove dust, which is an effective method for indoor pollution control and treatment.

4. Conclusions

In this work, a curtain purification system based on the combination of RR-TENG and a synergistic photocatalytic function for the degradation of VOCs has been proposed, providing a new method for air pollution control. The prepared highly active g-C_3N_4/TiO_2 composite photocatalyst was homogeneously loaded on the conductive fabric to fabricate the purification curtain. The high electrostatic field from RR-TENG enhances the formaldehyde adsorption and photocatalytic degradation efficiency, while it can also efficiently adsorb PM$_{2.5}$ simultaneously. In a simulated indoor environment, the formaldehyde removal rate of the system can reach 79.2% within 90 min, which is 13% higher than the result without TENG. Combined with the ESR technology, the working mechanism of the RR-TENG-enhanced photocatalytic degradation of formaldehyde is elaborated. Furthermore, in a simulated reaction chamber of 9 L, RR-TENG can rapidly reduce PM$_{2.5}$ from 999 μg m^{-3} to 50 μg m^{-3} within 60 s, which is only 1/21 of the natural precipitation time. When RR-TENG is run for 3 min, the dense smoke is quickly cleared in the reaction chamber. The system efficiently converts random energy into electricity and enhances the efficiency of photocatalysts. It realizes efficient treatment of air pollution caused by VOCs and PM and can provide an effective way to control indoor air pollution.

Author contributions

Dehong Yang: conceptualization, methodology, writing – original draft, data curation, software, and writing – review and editing. Zhaoqi Liu: conceptualization, methodology, writing – original draft, data curation, software, and writing – review and editing. Peng Yang: writing – review and editing. Ling Huang: writing – review and editing. Fengjiao Huang: writing – review and editing. Xinglin Tao: investigation. Yuxiang Shi: supervision. Rui Lei: visualization. Jiazhen Cao: writing – review and editing. Hexing Li: supervision. Xiangyu Chen: methodology, data curation, supervision, and writing – review and editing. Zhenfeng Bian: methodology, data curation, supervision, and writing – review and editing.

Conflicts of interest

There are no conflicts to declare.

Acknowledgements

References

1 Z. Dai, J. Zhu, J. Yan, J. Su, Y. Gao, X. Zhang, Q. Ke and G. N. Parsons, *Adv. Funct. Mater.*, 2020, **30**, 2001488.

2 T. Salthammer, S. Mentese and R. Marutzky, *Chem. Rev.*, 2010, **110**, 2536–2572.

3 M. Bohm, M. Z. Salem and J. Srba, *J. Hazard. Mater.*, 2012, **221–222**, 68–79.

4 B. O. Adebayo, J. Trautman, Q. Al-Naddaf, A. A. Rownaghi and F. Rezaei, *Environ. Sci. Technol.*, 2021, **55**, 9255–9265.

5 S. Xia, G. Zhang, Y. Meng, C. Yang, Z. Ni and J. Hu, *Appl. Catal., B*, 2020, **278**, 119266.

6 S. Weon, E. Choi, H. Kim, J. Y. Kim, H. J. Park, S. M. Kim, W. Kim and W. Choi, *Environ. Sci. Technol.*, 2018, **52**, 9330–9340.

7 H. Li, Z. Bian, J. Zhu, D. Zhang, G. Li, Y. Huo, H. Li and Y. Lu, *J. Am. Chem. Soc.*, 2007, **129**, 8406–8407.

8 J. Liu, P. Wang, W. Qu, H. Li, L. Shi and D. Zhang, *Appl. Catal., B*, 2019, **257**, 117880.

9 F. He, S. Weon, W. Jeon, M. W. Chung and W. Choi, *Nat. Commun.*, 2021, **12**, 6259.

10 J. Zhang, S. Wageh, A. Al-Ghamdi and J. Yu, *Appl. Catal., B*, 2016, **192**, 101–107.

11 H. L. Tan, R. Amal and Y. H. Ng, *J. Mater. Chem. A*, 2017, **5**, 16498–16521.

12 J. Lyu, L. Zhou, J. Shao, Z. Zhou, J. Gao, Y. Dong, Z. Wang and J. Li, *Chem. Eng. J.*, 2020, **391**, 123602.

13 C. Hu, S. Tu, N. Tian, T. Ma, Y. Zhang and H. Huang, *Angew. Chem., Int. Ed.*, 2021, **60**, 16309–16328.

14 W. Xu, H. Zheng, Y. Liu, X. Zhou, C. Zhang, Y. Song, X. Deng, M. Leung, Z. Yang, R. X. Xu, Z. L. Wang, X. C. Zeng and Z. Wang, *Nature*, 2020, **578**, 392–396.

15 Z. Liu, Y. Huang, Y. Shi, X. Tao, H. He, F. Chen, Z. X. Huang, Z. L. Wang, X. Chen and J. P. Qu, *Nat. Commun.*, 2022, **13**, 4083.

16 B. Chen, Y. Yang and Z. L. Wang, *Adv. Energy Mater.*, 2018, **8**, 1702649.

17 Z. Zhu, H. Xiang, Y. Zeng, J. Zhu, X. Cao, N. Wang and Z. L. Wang, *Nano Energy*, 2022, **93**, 106776.

18 Y. Feng, L. Ling, J. Nie, K. Han, X. Chen, Z. Bian, H. Li and Z. L. Wang, *ACS Nano*, 2017, **11**, 12411–12418.

19 Q. Fu, Y. Liu, J. Mo, Y. Lu, C. Cai, Z. Zhao, S. Wang and S. Nie, *ACS Nano*, 2021, **15**, 10577–10586.

20 J. Zhang, P. Chen, L. Zu, J. Yang, Y. Sun, H. Li, B. Chen and Z. L. Wang, *Small*, 2022, **18**, e2202835.

21 J. Mo, C. Zhang, Y. Lu, Y. Liu, N. Zhang, S. Wang and S. Nie, *Nano Energy*, 2020, **78**, 105357.

22 J. Yu, S. Wang, J. Low and W. Xiao, *Phys. Chem. Chem. Phys.*, 2013, **15**, 16883–16890.

23 A. Luengas, A. Barona, C. Hort, G. Gallastegui, V. Platel and A. Elias, *Rev. Environ. Sci. Biotechnol.*, 2015, **14**, 499–522.

24 J. Lelieveld, J. S. Evans, M. Fnais, D. Giannadaki and A. Pozzer, *Nature*, 2015, **525**, 367–371.

25 Z. Ren, L. Wu, Y. Pang, W. Zhang and R. Yang, *Nano Energy*, 2022, **100**, 107522.

26 X. Cao, Y. Jie, N. Wang and Z. L. Wang, *Adv. Energy Mater.*, 2016, **6**, 1600665.

27 H. Guo, J. Chen, L. Wang, A. C. Wang, Y. Li, C. An, J.-H. He, C. Hu, V. K. S. Hsiao and Z. L. Wang, *Nat. Sustain.*, 2020, **4**, 147–153.

28 K. Wang, W. Xu, W. Zhang, X. Wang, X. Yang, J. Li, H. Zhang, J. Li and Z. Wang, *Nano Res. Energy*, 2023, **2**, e9120042.

29 J. Qin, J. Wang, J. Yang, Y. Hu, M. Fu and D. Ye, *Appl. Catal., B*, 2020, **267**, 118667.

30 E. Ren, C. Zhang, D. Li, X. Pang and G. Liu, *View*, 2020, **1**, 20200052.

31 J. Zhang, Q. Xu, Z. Feng, M. Li and C. Li, *Angew. Chem., Int. Ed.*, 2008, **47**, 1766–1769.

32 J. Yan, F. Ye, Q. Dai, X. Ma, Z. Fang, L. Dai and C. Hu, *Nano Res. Energy*, 2022, DOI: **10.26599/nre.2023.9120047**.

33 B. Wang, M. Wang, F. Liu, Q. Zhang, S. Yao, X. Liu and F. Huang, *Angew. Chem., Int. Ed.*, 2020, **59**, 1914–1918.

34 S. H. Liu and W. X. Lin, *J. Hazard. Mater.*, 2019, **368**, 468–476.

35 M. Que, W. Cai, J. Chen, L. Zhu and Y. Yang, *Nanoscale*, 2021, **13**, 6692–6712.

36 R. Lei, Y. Shi, Y. Ding, J. Nie, S. Li, F. Wang, H. Zhai, X. Chen and Z. L. Wang, *Energy Environ. Sci.*, 2020, **13**, 2178–2190.

37 X. Li, C. Zhang, Y. Gao, Z. Zhao, Y. Hu, O. Yang, L. Liu, L. Zhou, J. Wang and Z. L. Wang, *Energy Environ. Sci.*, 2022, **15**, 1334–1345.

38 J. Luo and Z. L. Wang, *EcoMat*, 2020, **2**, e12059.

39 J. Han, Y. Feng, P. Chen, X. Liang, H. Pang, T. Jiang and Z. L. Wang, *Adv. Funct. Mater.*, 2022, **32**, 2108580.

40 R. Lei, S. Li, Y. Shi, P. Yang, X. Tao, H. Zhai, Z. L. Wang and X. Chen, *Adv. Energy Mater.*, 2022, **12**, 2201708.

41 P. Chen, J. An, S. Shu, R. Cheng, J. Nie, T. Jiang and Z. L. Wang, *Adv. Energy Mater.*, 2021, **11**, 2003066.

42 P. Yang, Y. Shi, S. Li, X. Tao, Z. Liu, X. Wang, Z. L. Wang and X. Chen, *ACS Nano*, 2022, **16**, 4654–4665.

43 S. Li, J. Nie, Y. Shi, X. Tao, F. Wang, J. Tian, S. Lin, X. Chen and Z. L. Wang, *Adv. Mater.*, 2020, **32**, e2001307.

44 W. Li, Z. Wei, K. Zhu, W. Wei, J. Yang, J. Jing, D. L. Phillips and Y. Zhu, *Appl. Catal., B*, 2022, **306**, 121142.

45 J. Mo, Y. Liu, Q. Fu, C. Cai, Y. Lu, W. Wu, Z. Zhao, H. Song, S. Wang and S. Nie, *Nano Energy*, 2022, **93**, 106842.

46 F. Dong, Z. Pang, Q. Lin, D. Wang, X. Ma, S. Song and S. Nie, *Nano Energy*, 2022, **100**, 107515.